corrosion and materials degradation

MDPI

Article

Reactivity of α-Alumina Powder and Fibres in Highly Alkaline Hydrothermal Solutions at 70 °C and 150 °C

Guillaume German [1,2,*], Emilie Perret [2], Francis Rebillat [1], Aurélien Debelle [3], Xavier Bourbon [3] and Jérôme Roger [1]

[1] Laboratoire des Composites Thermo Structuraux (LCTS), University of Bordeaux, 3 Allée de la Boétie, 33600 Pessac, France; rebillat@lcts.cnrs.fr (F.R.); roger@lcts.cnrs.fr (J.R.)
[2] High Performance Multifunctional Materials Domain, IRT Saint Exupéry, 3 Rue Tarfaya, 31400 Toulouse, France; emilie.perret@irt-saintexupery.com
[3] Agence Nationale pour la Gestion des Déchets Radioactifs (Andra), 1 Rue Jean Monnet, 92290 Châtenay-Malabry, France; aurelien.debelle@andra.fr (A.D.); xavier.bourbon@andra.fr (X.B.)
* Correspondence: german@lcts.cnrs.fr

Abstract

This research examines the hydrothermal corrosion behaviour of ceramic matrix composites (CMCs) under highly alkaline conditions (pH > 11.5) in the framework of a deep geological repository for high-level radioactive waste (HLW). The study focuses on the degradation of alumina powder and fibres, key constituents of an oxide/oxide CMC material. Accelerated ageing experiments were conducted in a highly alkaline aqueous environment (pH > 11.5, T = 70 °C for 220 days and T = 150 °C for 30 days). The research used a cross-disciplinary approach integrating thermodynamic calculations and physicochemical analyses to determine the degradation mechanisms of alumina powder and fibres induced by contact with the aqueous ageing solution. Characterisation of the aged alumina powders and fibres revealed the presence of unaltered alumina, hydrated alumina, amorphous phases, and calcium carbonate precipitates from the aqueous solution. Thermodynamic calculations indicate (1) the hydrolysis of alumina to diaspore and (2) the formation of an aluminosilicate phase and calcium carbonate. However, experimental results reveal kinetic limitations, such as the preferential formation of boehmite over diaspore, and morphology-dependent degradation pathways (protective-layer formation on fibres and partial dissolution of powders).

Keywords: Al_2O_3-based ceramic matrix composites; hydrothermal ageing; alumina powder degradation; alumina fibre degradation; alkaline environment; thermodynamic calculations

Check for updates

Academic Editor: Marina Cabrini

Received: 22 April 2026
Revised: 8 June 2026
Accepted: 16 June 2026
Published: 18 June 2026

Copyright: © 2026 by the authors. Licensee MDPI, Basel, Switzerland. This article is an open access article distributed under the terms and conditions of the Creative Commons Attribution (CC BY) license.

1. Introduction

In France, the management of radioactive waste is entrusted to the French National Radioactive Waste Management Agency (Andra). Under the *Cigéo* project (Centre industriel de stockage géologique) [1,2], high-level waste (HLW) and long-lived intermediate-level waste (LL-ILW) will be sent to a deep geological repository for reversible disposal. The repository will be built near Bure, on the border between the Meuse and Haute-Marne counties. The targeted host formation is the Callovo-Oxfordian claystone layer. This host rock, chosen specifically for its very low permeability, is at a depth of 420–550 m. If authorised, the repository will consist of approximately 15 km^2 of interconnected galleries and disposal micro-tunnels, or "cells", excavated at a depth of around 500 m. Each HLW cell, up to 150 m in length and about 75 cm (30 inches) in diameter, is designed to accommodate and, if necessary, allow the retrieval of waste packages.

To enable waste emplacement and potential retrieval, a cell lining is required. The reference material currently considered for this lining is low-carbon steel [3,4]. Under the expected in-service conditions—notably, anoxic environments in the presence of water—iron will corrode, leading to generalised corrosion and hydrogen generation. This H_2 (g) production is explicitly accounted for in Andra's 2023 licence application. However, gas management remains technically challenging and would necessitate complex active and passive mitigation measures. Regarding HLW disposal, operations are not expected to begin before 2080. In this context, Andra is exploring alternative materials to carbon steel that would minimise gas production while maintaining structural integrity.

Ceramic matrix composites (CMCs) have emerged as promising candidates for HLW cell liners due to their superior corrosion resistance in aggressive environments compared to metallic materials. In contrast to steel, oxide-based CMCs do not release H_2 gas, and its presence does not affect their stability. Originally developed for aerospace applications, oxide/oxide CMCs combine the physico-chemical stability of ceramics with the damage tolerance of fibre-reinforced architectures, ensuring structural integrity even in the event of local cracking—an advantage for safety-critical applications like Cigéo. Unlike monolithic ceramics, their non-brittle failure behaviour makes them particularly suitable for long-term confinement [5]. Additionally, alumina-based CMCs were selected here for their high chemical stability in corrosive environments and their relative ease of production compared to carbon-based materials, which are more prone to reactivity under such alkaline conditions. A recent study proposed an innovative "sandwich" design consisting of a monolithic ceramic tube with CMC skins on both the inner and outer surfaces [6]. To assess the feasibility of such a ceramic-based architecture for HLW cell liners, mechanical testing and numerical modelling are being developed [7]. However, although the mechanical properties of CMCs have been studied, their resistance to hydrothermal ageing in the presence of alkaline interstitial water (pH > 11.5) remains a significant gap in the literature.

In the *Cigéo* environment, temperatures are expected to remain below 90 °C, and the porewater is anticipated to be alkaline due to the interaction of groundwater with the cementitious grout injected at the interface between HLW cells and the geological medium [8]. Although the long-term behaviour of alumina-based CMCs under such alkaline conditions has not been studied in depth, the reactivity and phase transformations of alumina itself under similar conditions are documented in the literature. Previous studies investigating the reactivity of alumina powders in alkaline hydrothermal solutions have established several key findings. Under hydrothermal conditions, alumina undergoes hydration, forming polymorphs that depend on temperature, pressure, pH, and agitation. At temperatures below 100 °C, gibbsite (β–$Al(OH)_3$) or bayerite (α–$Al(OH)_3$) predominate [9–13], while boehmite (β–AlOOH) is prevalent between 100 and 375 °C at pressures below 10 MPa. High-pressure conditions (>10 MPa) favour diaspore (α–AlOOH) formation between 200 and 400 °C, and corundum (α–Al_2O_3) forms above 400 °C. pH and stirring also affect phase equilibria: at pH = 12, bayerite is stabilised without stirring, whereas boehmite forms with agitation [14]. Similarly, at room temperature and pH 7–11, bayerite predominates under stirring [15,16]. Overall, the equilibrium of alumina in aqueous solutions is sensitive to temperature, time, stirring, and solution composition.

This work aims to address this knowledge gap by investigating the reactivity and ageing mechanisms of α–alumina powders and fibres in highly alkaline hydrothermal solutions. However, our approach is not aimed at conducting a detailed kinetic study of the reactions or at fully elucidating the complex mechanisms involved. We focus on identifying the phenomena that occur on the surfaces of powders and fibres under these conditions, with particular emphasis on the thermodynamic characteristics that indicate the final state of the systems under consideration. The objectives are threefold. First, an

integrated approach combining ageing experiments, multi-technique characterisation of both solids and solutions, and thermodynamic calculations is developed. Second, both alumina powders and fibres—the fundamental constituents of oxide CMCs—are studied in order to assess the influence of morphology on reactivity. Third, the effect of temperature is examined at 70 °C and 150 °C, encompassing and exceeding the maximum repository temperature (≈90 °C). The influence of the initial solution composition is also investigated. Although the exact composition of the solution expected to be in contact with the HLW cell materials is not yet fully defined, a commonly used alkaline solution containing several dissolved mineral salts is considered [17]. The ageing experiments are conducted under static conditions at 70 °C to simulate repository storage conditions, while the dynamic ageing experiments (with stirring) at 150 °C are designed to enhance the reactivity between the solution and alumina, thereby accelerating degradation processes.

2. Materials and Methods

2.1. Thermodynamic Computations and Data

To support the experimental investigations, thermodynamic analyses of stable and metastable equilibria were performed with Thermo-Calc software *version 2025.a* [18]. The thermodynamic equilibria calculated with this software were based on the CALculation of PHAse Diagrams (CALPHAD) methodology [19]. Calculations were performed with the commercial Thermo-Calc databases (GCE2, TCAQ3, TCOX13) [20–22] and an additional database containing relevant thermodynamic descriptions of solid phases from the literature [23–34], as well as gaseous species [35]. Over 440 phases from the literature were considered for the calculations. A Python 3.11 code was developed using the TC-Python library to calculate the ageing equilibrium and the final equilibrium of alumina in a leaching solution between 20 °C and 200 °C [36]. Two types of calculations were performed: fixed-pressure calculations with P = 1 bar of N_2, 1 L of solution, and no gaseous species allowed to form, enabling calculations above 100 °C; and fixed-volume calculations with V = 1 L, free autogenous pressure, and formation of gaseous species with water evaporation (similar to the ageing experiments of the current work), with N_2 introduced to simulate anaerobic and experimental conditions. The fixed-pressure calculations (1 bar of N_2, no gaseous species) were designed to replicate the experimental series, as the gas volume in the reactors was minimal due to near-total solution filling. Fixed-volume calculations confirmed that the autogenous pressure of water vapour has a negligible influence on condensed phases, validating the fixed-pressure approach under these conditions. The quantities extracted from the thermodynamic calculations are the masses of the solid phases formed, the pH, the partial pressures of the gases, and the Gibbs energy (ΔG).

2.2. Methodology to Determine the Behaviour Under Hydrothermal Conditions

Four series of experiments were conducted in separate reactors using two distinct material morphologies. The objective was to evaluate the influence of the aqueous solution on the alumina materials (powder and fibres) employed in the formulation of the oxide composite.

In the initial series of aged powder at 70 °C, called ***P70***, 4 g of α-alumina powder (from Baikowski, 99.99% pure, grain size of 150 nm, specific surface area $S_{alumina}$ = 10 $m^2 \cdot g^{-1}$, as measured by BET, was employed as the primary constituent of the composite matrix. The powder was introduced into a 100 mL PTFE reactor and combined with 100 g of the aqueous solution prepared with Milli-Q® water (resistivity = 18.2 MΩ·cm).

In a second series composed of aged fibres at 70 °C, called ***F70***, 4 g of an α-alumina woven fabric (from 3M Nextel 610, with a purity of over 99%, containing 0.7 $\%_{mass}$ of Fe_2O_3 and 0.3 $\%_{mass}$ of SiO_2, fibre diameter of 12 µm) was introduced into a 500 mL

PTFE reactor and combined with 500 g of the same aqueous solution. Both reactors were hermetically closed, with a filling ratio close to 100 % to minimise gas formation. This leaching solution was prepared inside a glove box in a controlled atmosphere ($N_{2(g)}$) and by dissolving the salts listed in Table 1 one by one. Table 1 also summarises the corresponding ionic composition.

Table 1. Salts used to prepare the leaching solution.

Salt	Mass/g	Purity/%	Provider
KCl	0.00075	>99.5	Sigma-Aldrich, St. Louis, MO, USA
K_2SO_4	4.36086	>99	Sigma-Aldrich, St. Louis, MO, USA
$Al_2(SO_4)_3 \cdot 18H_2O$	0.13738	>97	Sigma-Aldrich, St. Louis, MO, USA
$CaSO_4 \cdot 2H_2O$	1.35694	>99	Sigma-Aldrich, St. Louis, MO, USA
$Na_2SiO_3 \cdot 5H_2O$	0.61393	>95	Sigma-Aldrich, St. Louis, MO, USA
$NaHCO_3$	1.05181	>99.5	Sigma-Aldrich, St. Louis, MO, USA
NaOH	≈0.4	>98.5	Sigma-Aldrich, St. Louis, MO, USA

Ions	K^+	Na^+	Ca^{2+}	Si[IV]	Al[III]	SO_4^{2-}	CO_3^{2-}
Concentration/mol·L^{-1}	0.05006	0.02711	0.00788	0.00290	0.00041	0.03353	0.01252

The pH was adjusted to 11.2 at 50 °C by the addition of sodium hydroxide ([NaOH] = 1 mol·L^{-1}). The reactors for experiments P70 and F70 were placed in an oven without stirring at a temperature of 70 °C for an ageing duration of up to 220 days.

After 220 days at 70 °C, these reactors were opened in a glove box with an oxygen concentration below 2 ppm to prevent carbonation of the samples. The solid by-products were then dried under nitrogen inside the glove box.

Series ***P150*** and ***F150*** consisted of evaluating the ageing of alumina powder and alumina fibres, using the same protocol as that used for ***P70*** and ***F70***, in pressurised reactors with PTFE tanks at a temperature of 150 °C and an autogenous pressure of up to 6 bars, with stirring at 200 RPM. For ***P150***, 8 g of α-alumina powder was introduced into a 200 mL PTFE reactor, whereas for ***F150***, 4 g of alumina woven fabric was introduced into a 500 mL PTFE reactor. Both were combined with the aqueous solution at a filling ratio close to 100%. Powder from ***P150*** was extracted after 30, 65, 80, and 120 days to monitor ageing. The fibres from ***F150*** were extracted after 30 days of ageing.

A parallel experiment (***S70***) was conducted on the aqueous solution alone, with the objective of determining its evolution with temperature over time. To this end, 100 ml of aqueous solution was exposed to the conditions of series ***P70*** for a duration of up to 220 days.

2.3. Characterisation Techniques

After 220 days, the remaining solutions of series ***P70*** and ***F70*** were extracted to analyse the aqueous species present in the aged solutions and to compare them with the species initially introduced into the mixture. Precipitated phases were isolated through evaporation of the residual liquid. The liquid from each experiment was analysed by inductively coupled plasma atomic emission spectroscopy (ICP-AES, iCAP PRO Duo-Thermo Scientific, Waltham, MA, USA).

The collected precipitated phases were analysed by X-ray diffraction (XRD, Bruker D8 Advance diffractometer, Karlsruhe, Germany using a Cu Kα anticathode).

The surfaces of the formed particles were observed by scanning electron microscopy (SEM, FEI Quanta 400FEG, Thermo Fisher Scientific, Hillsboro, OR, USA) operating at 5 kV and equipped with an energy-dispersive X-ray spectroscopy (EDX, Ultim Max, Oxford Instruments, Abingdon, UK) detector, and by transmission electron microscopy (TEM,

JEOL JEM 2200FS FEG HR 200 kV high-resolution camera, Tokyo, Japan) equipped with an EDX detector. Finally, the outermost surface of the alumina fibres was analysed by X-ray photoelectron spectroscopy (XPS, K-α Thermo Fisher, Waltham, MA, USA).

3. Results

3.1. Thermodynamic Calculations on the Solid–Liquid Equilibria

As mentioned in the Introduction, different hydrated phases of alumina can be formed depending on the experimental conditions. However, the most thermodynamically stable hydrated phase is diaspore. Indeed, it has the lowest Gibbs free energy formation per mole of atoms. This suggests that the phases observed in the literature are in a metastable state, unable to reach the thermodynamic equilibrium with the lowest energy. It was therefore chosen to compare two situations during thermodynamic calculations to determine the expected evolution of these systems. Two systems were considered: a stable system in which diaspore can form and a metastable system in which it cannot. For all calculations, the chemical compositions were those of the experiments for 1 L, and the introduced amount of alumina was adapted to correspond to the identified molar fraction ($x_{Al_2O_3}$ = 0 and $x_{Al_2O_3}$ = 0.05). The molar fraction of $x_{Al_2O_3}$ = 0.05 corresponds to the quantity of alumina used in experiments ***P70*** and ***P150***. However, the calculations are based on the assumption that all of the introduced Al_2O_3 interacts with the leaching solution. Yet, during the experiments, only a thin layer of the powder is actually in contact with the medium, which complicates the determination of the molar fraction actually involved in the solid/liquid exchanges.

3.1.1. Solid Phases Formed in the Process

Solid Phases Formed from the Initial Aqueous Solutions

As illustrated in Figure 1, predictions for both the stable system with possible diaspore formation (a) and the metastable system without diaspore formation (b) for 1 L of the initial leaching solution ($x_{Al_2O_3}$ = 0) indicate the precipitation of several solids across the temperature range from 20 to 200 °C. In both cases, the predominant phases are sodium sulfate (Na_2SO_4), gypsum ($CaSO_4{\cdot}2H_2O$), and dicalcium silicate (Ca_2SiO_4), whose quantities follow similar trends with temperature. At 70 °C, the mass of Na_2SO_4 is 1900 mg in the stable system and slightly lower at 1860 mg at 150 °C, with comparable values observed in the metastable case. For gypsum and dicalcium silicate, their quantities remain stable up to 70 °C (850 mg and 380 mg, respectively), then decrease and stabilise at 790 mg and 330 mg above this temperature in both scenarios. In the stable system (a), the aluminosilicate phase forms above 100 °C with a constant quantity of 100 mg, decreasing below 100 °C, and disappearing at 70 °C. In contrast, in the metastable system (b), its formation is predicted over a wider temperature range, with 30 mg present at 70 °C. Finally, in the stable case, the remainder of the aluminium present in the initial aqueous solution is transformed into diaspore (α–AlOOH), with a quantity that remains stable between 20 °C and 70 °C (23 mg) but then decreases and disappears above 102 °C. In the metastable case, the hydrated phase is boehmite (β–AlOOH), a polymorph of diaspore with a similar temperature stability range but a lower quantity (14 mg) at 70 °C, and then disappearing at 92 °C.

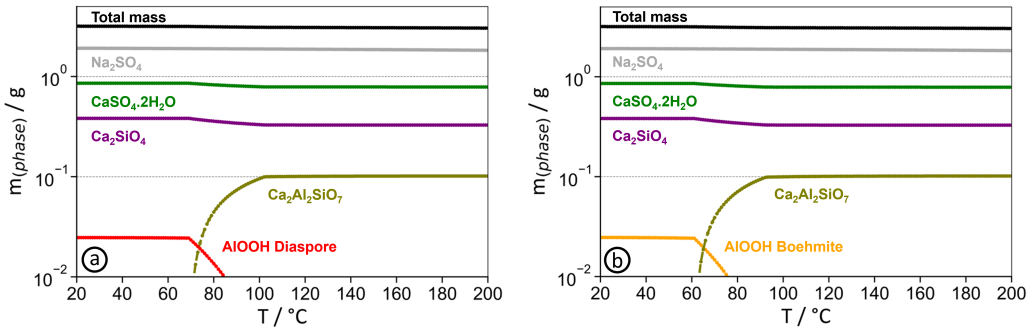


Figure 1. Solid phases formed between 20 and 200 °C at P = 1 bar under a N_2 atmosphere for $x_{Al_2O_3}$ = 0 (initial leaching solution without alumina). (**a**) Stable system: diaspore formation allowed. (**b**) Metastable system: diaspore formation forbidden. (One calculation point per degree).

Solid Phases Formed for the Alumina Powder in Contact with the Initial Aqueous Solution

As shown in Figure 2, predictions considering alumina powder in both the stable (a) and metastable (b) systems in contact with the initial leaching solution ($x_{Al_2O_3}$ = 0.05) indicate the precipitation of several solid phases over the temperature range of 20 to 200 °C. In both systems, the introduced alumina is transformed into a hydrated aluminium oxide: diaspore (α–AlOOH) in the stable case and boehmite (β–AlOOH) in the metastable case, with similar quantities of 209 g throughout most of the temperature range. The formation of sodium sulfate (Na_2SO_4) remains consistent between the two systems, following the same trend as in the case without alumina addition: 1900 mg at 70 °C, decreasing slightly to 1860 mg at 150 °C. Calcium sulfate ($CaSO_4 \cdot 2H_2O$) and dicalcium silicate (Ca_2SiO_4) exhibit stable quantities up to 70 °C in both scenarios (840 mg and 370 mg, respectively), followed by a gradual decline with increasing temperature. At 150 °C, their respective masses decrease to 730 mg and 290 mg. For the aluminosilicate phase, in the stable case, its quantity decreases from 170 mg at 150 °C to 2.9 mg at 70 °C and then disappears completely. In the metastable case, the decrease is less pronounced, from 190 mg at 150 °C to just 38 mg at 70 °C, with disappearance at around 63 °C.

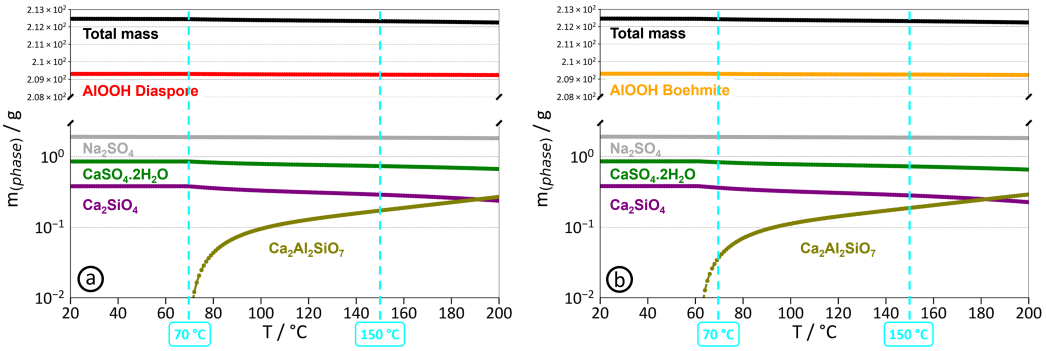


Figure 2. Solid phases formed between 20 and 200 °C at P = 1 bar under a N_2 atmosphere for $x_{Al_2O_3}$ = 0.05 (alumina powder in contact with leaching solution). (**a**) Stable system: diaspore formation allowed. (**b**) Metastable system: diaspore formation forbidden. (One calculation point per degree).

Solid Phases Formed for the Alumina Fibres in Contact with the Initial Aqueous Solution

As shown in Figure 3, the predictions for both the stable (a) and metastable (b) systems for alumina fibres in contact with the initial leaching solution ($x_{Al_2O_3} + x_{SiO_2} = 0.05$) indicate the precipitation of multiple solid phases over the temperature range from 20 to 200 °C. In both systems, the introduced alumina is transformed into a hydrated aluminium oxide: diaspore (α–AlOOH) in the stable case and boehmite (β–AlOOH) in the metastable case, with comparable quantities of approximately 209 g throughout most of the temperature

range. Above 155 °C, the mass of the hydrate decreases slightly and stabilises at 208 g above 160 °C. Sodium sulfate (Na_2SO_4) shows a similar trend in both systems, with a quantity of 1900 mg at 70 °C decreasing gradually to 1860 mg at 150 °C. Above 155 °C, its mass declines more rapidly, reaching 1570 mg at 160 °C and remaining constant thereafter. Dicalcium silicate (Ca_2SiO_4) is also consistently present across the full temperature range at a stable quantity of 1030 mg in both cases. The cementitious phase labelled "C4AsH12" (formulated as $CaO{\cdot}Al_2O_2{\cdot}CaSO_4{\cdot}12H_2O$) appears in both systems over the temperature range. Its quantity decreases from 20 °C to 155 °C, then increases slightly up to 160 °C, and stabilises at 40 mg. At 70 °C, its quantity is 28 mg in both systems and decreases to 25 mg by 150 °C. Carnegieite ($NaAlSiO_4$), a sodium aluminosilicate phase, forms at temperatures above 150 °C. Its mass remains stable at 580 mg up to 155 °C, after which it disappears abruptly, at 155 °C in the stable case and slightly earlier in the metastable case at 153 °C. Muscovite ($KAl_2(Si_3Al)O_{10}(OH)_2$) appears at low temperatures in both systems, from 20 °C to 42 °C. In the stable system, its mass decreases from 350 mg to 50 mg, while in the metastable system, it decreases from 480 mg to 190 mg. Following the disappearance of muscovite, kaolinite ($Al_2O_3{\cdot}2SiO_2{\cdot}2H_2O$) forms in both cases. In the stable system, kaolinite disappears at around 54 °C, whereas in the metastable case, it persists up to 101 °C.

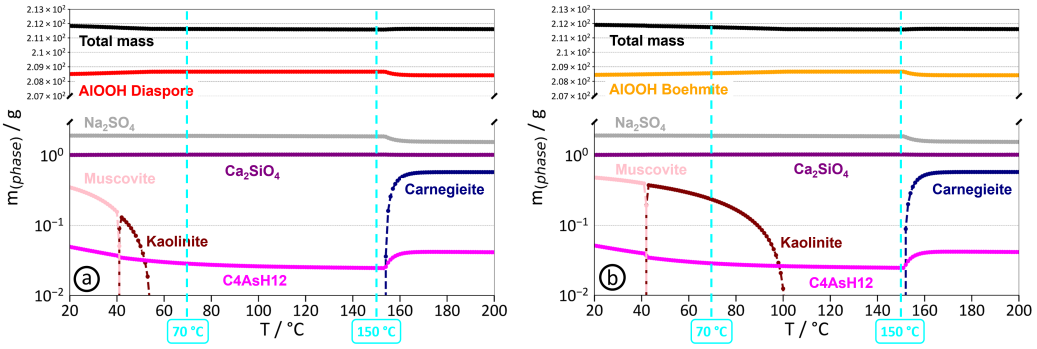


Figure 3. Solid phases formed between 20 and 200 °C at P = 1 bar under N_2 atmosphere for $x_{Al_2O_3} + x_{SiO_2} = 0.05$ (alumina fibres in contact with leaching solution). (**a**) Stable system: diaspore formation allowed. (**b**) Metastable system: diaspore formation forbidden. (One calculation point per degree).

3.1.2. Formation of Aqueous Species

Aqueous Species Formed from the Initial Aqueous Solutions

As shown in Figure 4, the speciation of the aqueous solution without any solid addition reveals consistent trends between the stable and metastable systems. For carbonate species (Figure 4a,d), CO_3^{2-}, $NaCO_3^-$, and $NaHCO_3$ decrease with increasing temperature, whereas H_2CO_3 increases and HCO_3^- remains relatively stable. For sulfate species (Figure 4b,e), SO_4^{2-} decreases gradually, whereas KSO_4^- and $NaSO_4^-$ increase between 70 °C and 150 °C. For other species (Figure 4c,f), K^+ and Cl^- remain constant across the temperature range, Na^+ shows a gradual increase, and OH^- and AlO_2^- show inflection points at 60 °C (metastable) and 70 °C (stable), followed by further inflection points at 90 °C and 100 °C, respectively. Finally, H^+ appears above 120 °C in both cases. These shifts reflect changes in chemical equilibria induced by the presence or absence of solid phases, as illustrated in Figure 1.

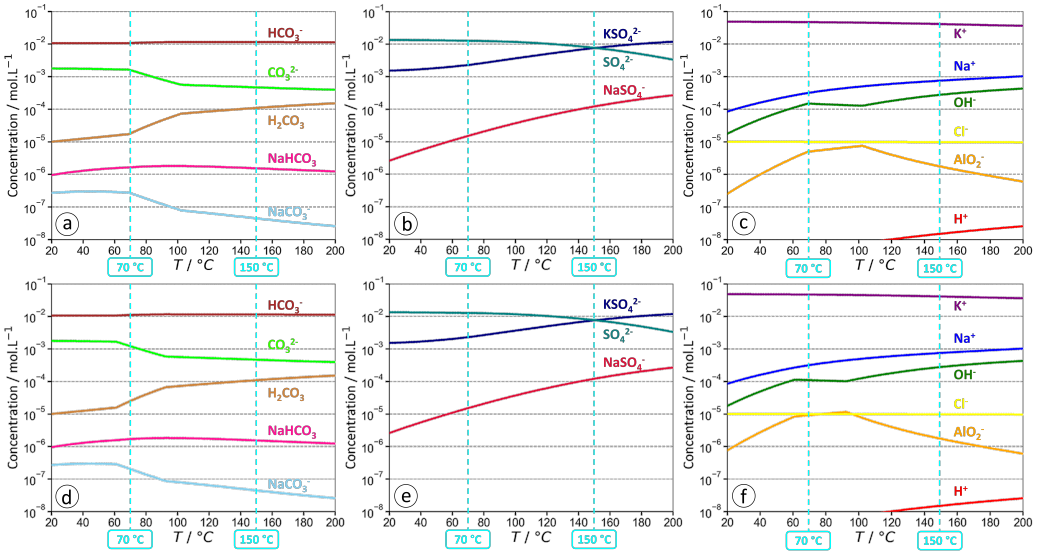


Figure 4. Concentrations of aqueous species formed between 20 and 200 °C at P = 1 bar for $x_{Al_2O_3} = 0$ (initial leaching solution without alumina). Stable system: (**a**) carbonate species, (**b**) sulfate species, (**c**) other species. Metastable system: (**d**) carbonate species, (**e**) sulfate species, (**f**) other species. (One calculation point per degree).

Aqueous Species for the System with Alumina Powder in Contact with the Initial Aqueous Solution

As shown in Figure 5, the speciation of the aqueous solution with alumina powder ($x_{Al_2O_3} = 0.05$) reveals trends similar to those in Figure 4 but with notable differences due to the addition of alumina. For carbonate species (Figure 5a,d), CO_3^{2-} and $NaCO_3^-$ exhibit a marked decrease with increasing temperature, with their concentrations being 3 and 150 times lower at 150 °C, respectively, compared to $x_{Al_2O_3} = 0$. H_2CO_3 is comparable to Figure 4 at 70 °C, but the quantity is 3 times higher at 150 °C after the addition of $x_{Al_2O_3} = 0.05$ in both cases. HCO_3^- and $NaHCO_3$ remain stable, similar to the aqueous solution alone (Figure 4). For sulfate species (Figure 5b,e), SO_4^{2-}, $NaSO_4^-$, and KSO_4^- follow a similar trend to that in Figure 4. For other species (Figure 5c,f), K^+ and Cl^- remain constant, Na^+ shows a gradual increase, and the concentration of AlO_2^- is comparable to that in Figure 4 at 70 °C but is 10 times higher at 150 °C after alumina addition. The concentration of OH^- is 3 times lower at 150 °C, whereas the concentration of H^+ is 3 times higher.

Aqueous Species for the System with Alumina Fibres in Contact with the Initial Aqueous Solution

As shown in Figure 6, the general trends in aqueous speciation are consistent between the stable and metastable systems. For carbonate species (Figure 6a,e), CO_3^{2-}, HCO_3^-, and $NaHCO_3$ show a marked decrease with increasing temperature, whereas H_2CO_3 remains constant. For sulfate species (Figure 6b,f), SO_4^{2-}, KSO_4^-, and $NaSO_4^-$ show the same behaviour as the alumina powder system (Figure 5). For silicate species (Figure 6c,g), H_4SiO_4, H_2SiO_3, and H_8SiO_6 show an earlier plateau in the stable case, followed by a decline in both systems above 150 °C. For other species (Figure 6d,h), K^+ and Cl^- remain stable, Na^+ shows a progressive increase, and the concentration of AlO_2^- appears above 188 °C in the stable case but emerges at 146 °C in the metastable case, indicating a premature destabilisation of the solid aluminium phase. Finally, the concentration of H^+ increases gradually with temperature in both systems, indicating acidification of the solution in the presence of silicon. The acidification observed could be attributed to the dissociation of the silicate network in an alkaline environment and to the deprotonation of the Si-OH groups [37,38].

Thermodynamic calculations were also performed by fixing the volume and varying the pressure. The results obtained are equivalent to those obtained at fixed pressure. This means that at these temperatures and pressures, the systems' equilibria are not influenced by pressure or volume parameters.

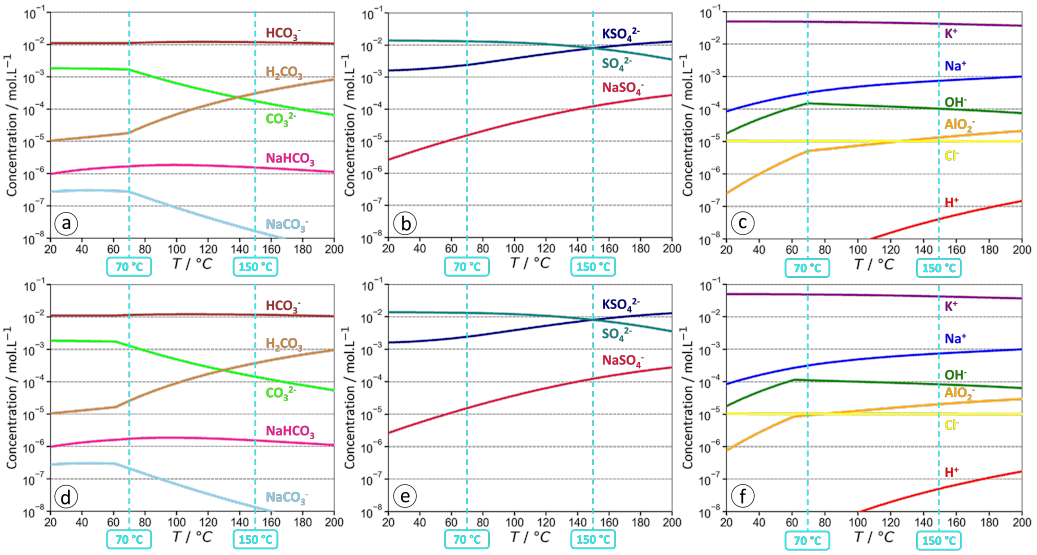


Figure 5. Concentrations of aqueous species formed between 20 and 200 °C at P = 1 bar for $x_{Al_2O_3} = 0.05$ (alumina powder in contact with leaching solution). Stable system: (**a**) carbonate species, (**b**) sulfate species, (**c**) other species. Metastable system: (**d**) carbonate species, (**e**) sulfate species, (**f**) other species. (One calculation point per degree).

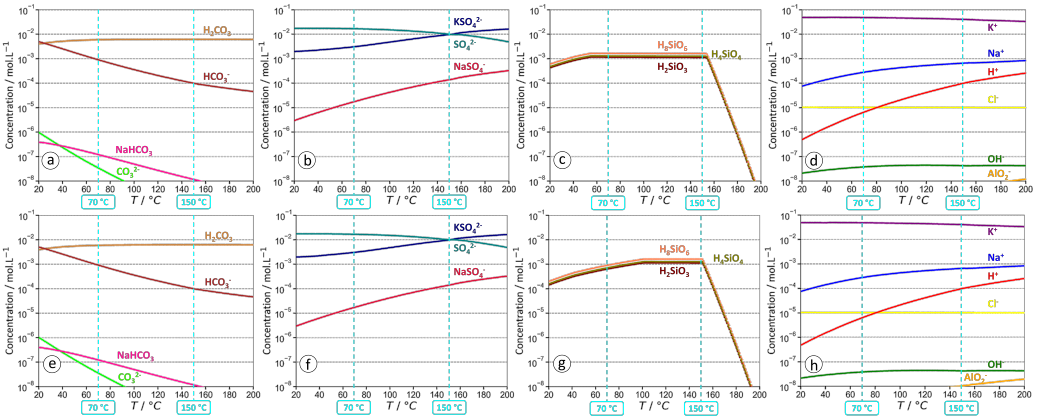


Figure 6. Concentrations of aqueous species formed between 20 and 200 °C at P = 1 bar for $x_{Al_2O_3} + x_{SiO_2} = 0.05$ (alumina fibres in contact with leaching solution). Stable system: (**a**) carbonate species, (**b**) sulfate species, (**c**) silicate species, (**d**) other species. Metastable system: (**e**) carbonate species, (**f**) sulfate species, (**g**) silicate species, (**h**) other species. (One calculation point per degree).

3.2. Characterisation of Initial and Aged Samples

3.2.1. Evolution of the Composition of the Initial Leaching Solution

In this section, the experimental evolution of the aqueous solution (***S70***, ***P70***, ***F70***) is compared to thermodynamic calculations performed for the solution alone ($x_{Al_2O_3} = 0$). This comparison highlights the impact of alumina powder and fibres on the solution chemistry.

Figure 7 illustrates the chemical composition of the initial leaching solution after ageing in the ***S70*** experiments with a constant volume of 100 mL. The very low concentration of calcium (Figure 7a) in the solution demonstrates that the majority has precipitated (7.88 mmol·L^{-1} was introduced, and only 0.035±0.002 mmol·L^{-1} remains in solution) and

has decreased over time. The thermodynamic calculations show that the concentration of calcium should reach 2×10^{-9} mmol·L^{-1} at equilibrium. In the case of potassium (Figure 7b), the concentration remains practically constant, going from 50 mmol·L^{-1} initially to 47 ± 9 mmol·L^{-1} after 220 days. Previously, the thermodynamic calculations showed that the concentration of potassium should reach 49.8 mmol·L^{-1} at equilibrium. Similarly, the observation is consistent for sodium (Figure 7c): 96% of it is still in solution (33.31 mmol·L^{-1} initially introduced and 32 ± 3 mmol·L^{-1} is present at t = 0). The remaining fraction is precipitated. The thermodynamic calculations show that the concentration of sodium should reach 0.368 mmol·L^{-1} at equilibrium. For aluminium (Figure 7d), 0.033 ± 0.002 mmol·L^{-1} out of the 0.4 mmol·L^{-1} introduced remains in solution and increases slightly over time (0.060 ± 0.003 mmol·L^{-1} after 220 days of ageing). The remaining 92% of aluminium is precipitated in the solid part. The thermodynamic calculations show that the concentration of aluminium should reach 6×10^{-3} mmol·L^{-1} at equilibrium, taking into account the volume variation of the solution. In the case of silicon (Figure 7e), 72% of the initial amount (2.9 mmol·L^{-1}) remains in solution (2.1 ± 0.1 mmol·L^{-1}). Moreover, the concentration of silicon increases slightly over time, up to 2.3 ± 0.1 mmol·L^{-1} after 220 days. In parallel, the thermodynamic calculations show that the concentration of silicon should reach zero at equilibrium.

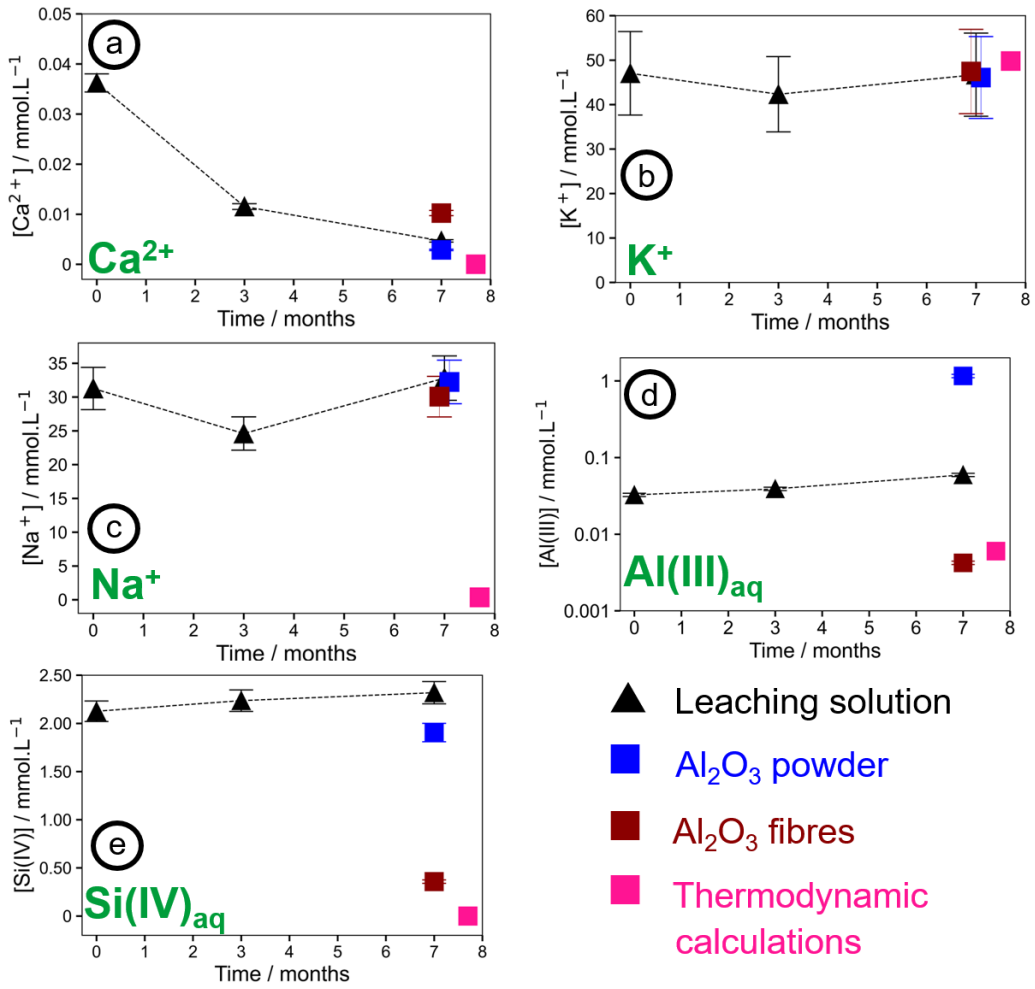


Figure 7. Time evolution of the aqueous solution after 220 days at 70 °C for experiments ***P70*** and ***F70***, together with the time evolution of the initial aqueous solution at 0, 90, and 220 days, showing the total dissolved content and the thermodynamic quantities of different ions: (**a**) Ca^{2+}, (**b**) K^{+}, (**c**) Na^{+}, (**d**) Al (III), and (**e**) Si (IV). Error bars are 5% for Al (III), Ca^{2+}, and Si (IV); 10% for Na^{+}; and 20% for K^{+}.

The experimental values shown in Figure 7 are summarized in Table 2

Table 2. Evolution of species concentrations over time in experiments ***S70***, ***P70***, and ***F70*** compared to thermodynamic calculations.

	[Ca(II)]/mmol/L	[K(I)]/mmol/L	[Na(I)]/mmol/L	[Al(III)]/mmol/L	[Si(IV)]/mmol/L
S70 (t = 0)	0.035	47	32	0.033	2.1
S70 (t = 3 months)	0.012	42	24.6	0.039	2.2
S70 (t = 7 months)	0.005	47	32	0.059	2.3
P70 (t = 7 months)	0.003	46	32	1.16	1.9
F70 (t = 7 months)	0.010	47	30	0.004	0.36
Thermodynamic	2×10^{-9}	49.8	0.368	6×10^{-3}	0

The pH evolution of the aqueous solution alone at 70 °C is shown in Figure 8a. The initial pH was 10.88 (compared to 11.2 during preparation) and decreased to 9.87 after 220 days. A rapid drop was observed within the first three days, with the pH reaching 10.6, followed by a slower decline. As illustrated in Figure 8b, the pH did not reach thermodynamic equilibrium, which is predicted to be 8.74 at 70 °C.

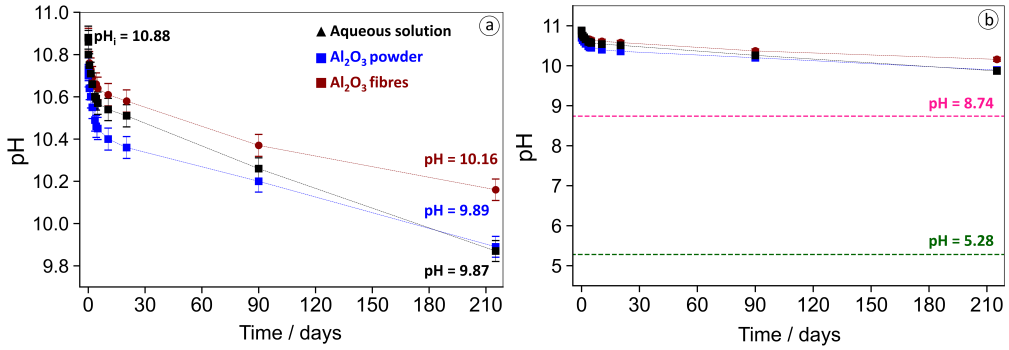


Figure 8. pH evolution and thermodynamic equilibrium predictions for alumina-based systems at 70 °C. (**a**) Experimental pH evolution of the aqueous solution alone (black triangles), in contact with alumina powder (blue squares), and in contact with alumina fibres (red squares) over 220 days. (**b**) Comparison of experimental pH values with thermodynamic equilibrium predictions: aqueous solution alone and powder/aqueous solution (pink dashed line, pH = 8.74), and fibres/aqueous solution (green dashed line, pH = 5.28).

Figure 9 shows that the initial neoformed precipitate (m = 598 mg) consists of an amorphous nanonetwork of aluminosilicate particles with an Al/Si atomic ratio of 17/83. The larger precipitated grains (top right) are composed of calcium carbonate ($CaCO_3$). Figure 1 shows that thermodynamically, the quantity of the solid phase formed from the initial solution is m = 3164 mg.

The initial neoformed precipitate from experiment *S70* (aqueous solution alone, 70 °C, 220 days) was characterised by TEM-EDX (Figure 9). The analysis reveals an amorphous aluminosilicate nanonetwork with an Al/Si atomic ratio of 17/83, indicating the precipitation of silicon and aluminium species from the solution. Larger precipitated grains, identified as calcium carbonate ($CaCO_3$), are also observed in the top right of Figure 9. The total mass of the precipitate was measured as m = 598 mg. For comparison, thermodynamic calculations (Figure 1) predict a total solid phase mass of m = 3164 mg under equilibrium conditions, highlighting a significant discrepancy between experimental observations and theoretical predictions.

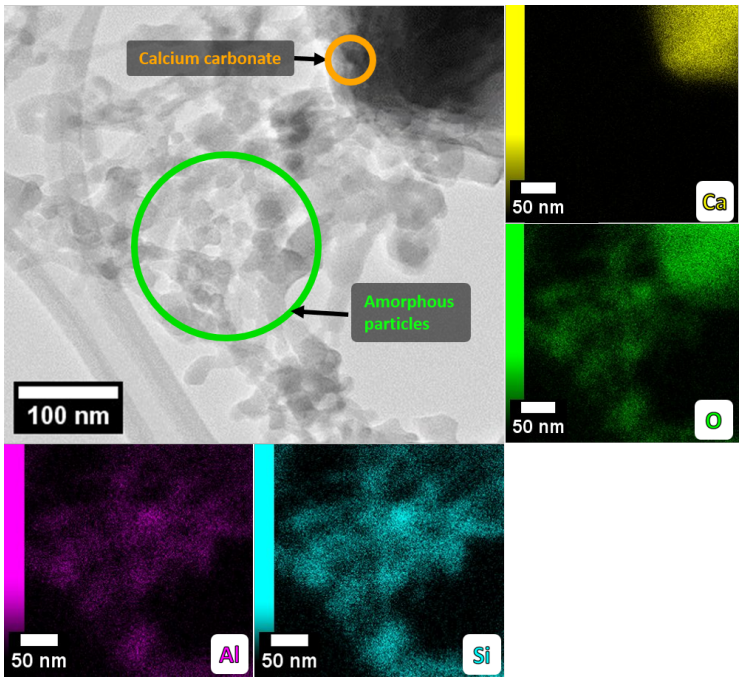


Figure 9. TEM-EDX analysis of initial precipitate from experiment ***S70*** (aqueous solution alone, 70 °C, 220 days). Presence of an amorphous aluminosilicate nanonetwork (Al/Si atomic ratio = 17/83) and calcium carbonate ($CaCO_3$) grains.

3.2.2. Ageing Test on Alumina Powder

The concentrations of the different species in the aqueous solution analysed by ICP (Figure 7) are affected differently by the presence of the alumina powder in experiment ***P70***. Calcium, potassium, and sodium concentrations are equivalent to those in the initial aqueous solution. The silicon concentration decreases over time, from 2.1 mmol·L^{-1} to 1.9 ± 0.1 mmol·L^{-1}. The aluminium concentration is 28 times higher than initially, increasing from 0.04 mmol·L^{-1} to 1.2 ± 0.1 mmol·L^{-1}. The additional Al comes from the alumina powder: 0.84 mmol·L^{-1} dissolved in the aqueous solution, representing 1 $\%_{mol}$ of Al from the introduced alumina powder.

Figure 8a shows that the pH of the aqueous solution in contact with the alumina powder followed a trend nearly identical to that of the solution alone during the first three days. However, it subsequently decreased more rapidly, reaching pH 10.4 after 20 days, while the solution alone remained at pH 10.55. This trend slowed afterward, and at 220 days, the pH values were nearly identical (9.89 for the powder system). As shown in Figure 8b, thermodynamic equilibrium was also not achieved in this system.

Figure 10 presents a comparative analysis of the X-ray diffractograms of the precipitated phases formed during the preparation of the initial leaching solution (Figure 10a), the alumina aged for 35 days at 150 °C in experiment ***P150*** (Figure 10b), the alumina aged for 220 days at 70 °C in experiment ***P70*** (Figure 10c), and the initial alumina (Figure 10d). The initial precipitate from the initial solution exhibits the presence of two distinct crystalline phases: the $CaCO_3$ phase and the $KNaSO_4$ phase. The amorphous aluminosilicate phase observed in Figure 9 may not produce a distinct signal in the XRD analysis of sample ***S70*** due to its low concentration and amorphous nature, which could cause it to get lost in the background noise. The diffractogram of the aged alumina (***P70***) can be considered a sum of the patterns corresponding to both the initial precipitate and the initial alumina. The same observation holds for the alumina powder in experiment ***P150***, with an additional phase observed, identified as boehmite (β–AlOOH). There is no detection of a diaspore phase (α–AlOOH) in the diffractogram, meaning that the system is in ortho-equilibrium.

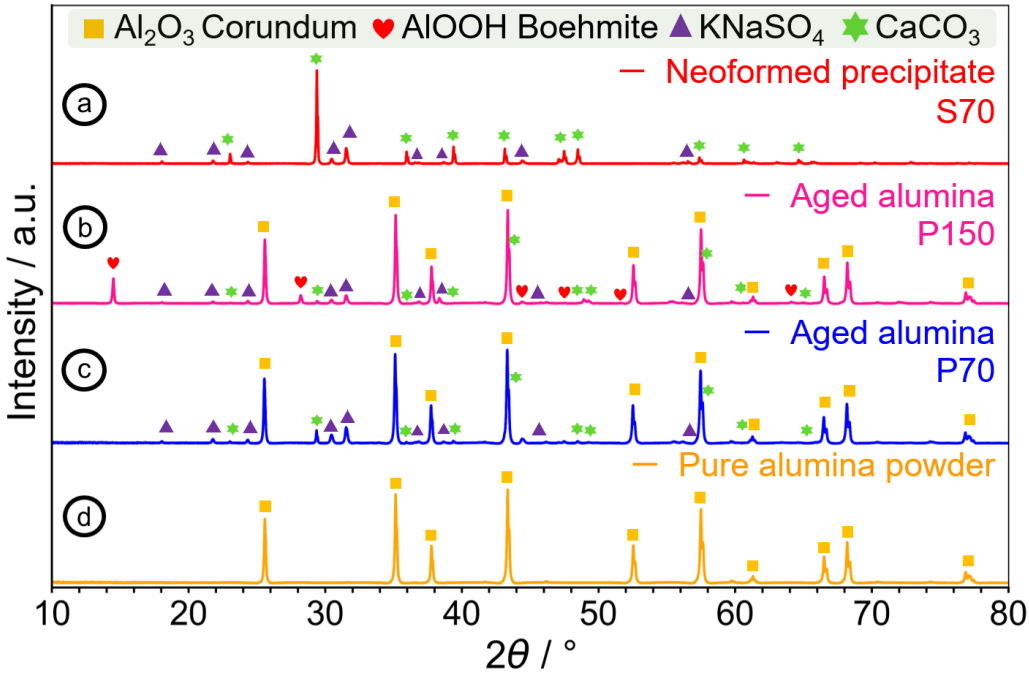


Figure 10. XRD patterns of solid phases: (**a**) initial precipitate from ***S70***, (**b**) alumina aged for 220 days at 70 °C in experiment ***P70***, (**c**) alumina aged for 30 days at 150 °C in experiment ***P150***, and (**d**) initial alumina powder (K_α Cu).

Post-treatement with Rietveld refinement (Figure 11) of the XRD of the aged alumina at 150 °C in experiment ***P150*** as a function of ageing time shows that the amount of boehmite phase increases with ageing duration.

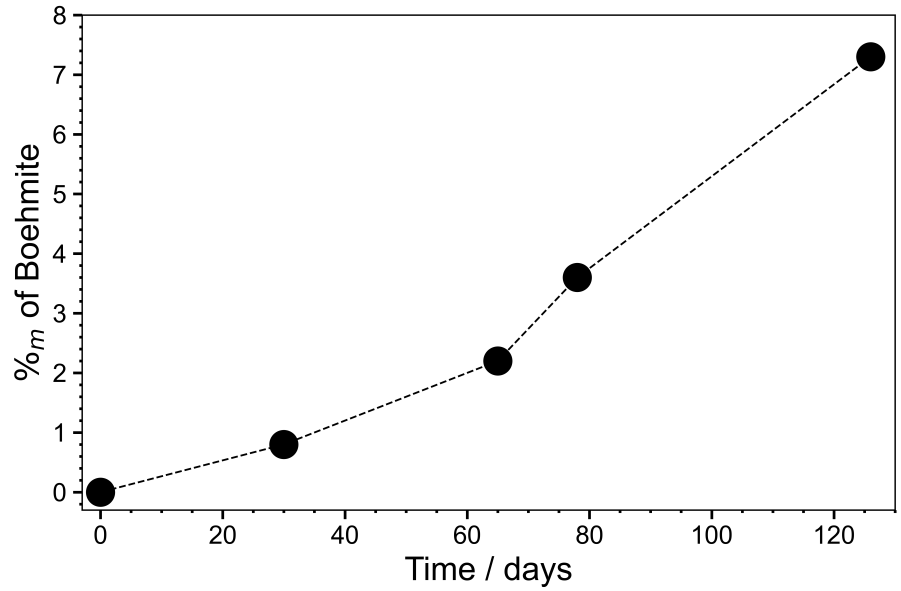


Figure 11. Rietveld refinement of XRD patterns for experiment ***P150*** (150 °C, stirred conditions). Evolution of boehmite (β–AlOOH) phase fraction with ageing time, compared to alumina.

Figure 12 shows the SEM images of the formed solids in the different experiments. The initial powder (Figure 12a) is composed of alumina grains with an average size of 150 nm, as expected from the datasheet. The powder aged for 30 days at 150 °C in experiment ***P150*** (Figure 12b) contains initial raw alumina grains, but some new grains appear with a pellet-like morphology corresponding to the boehmite phase, as shown in Figure 13. The powder aged for 220 days at 70 °C in experiment ***P70*** (Figure 12c) contains alumina grains covered with some aqueous amorphous hydrated phase. EDX analyses corresponding to the gelatinous area (circled zone) show amorphous grains composed of oxygen, aluminium, and carbon, as well as sulfur and potassium, with an atomic ratio of O:Al:C:S:K = 57:14:21:3:5. The solid formed after 220 days at 70 °C in experiment ***P70*** is also composed of the neoformed precipitate corresponding to the circled zone in Figure 12d, identified as calcium carbonate grains with an atomic ratio obtained by EDX analysis: Ca:C:O = 20:26:54. Theoretically, this ratio should be 20:20:54, but accurate quantification of carbon and oxygen by EDX is not straightforward.

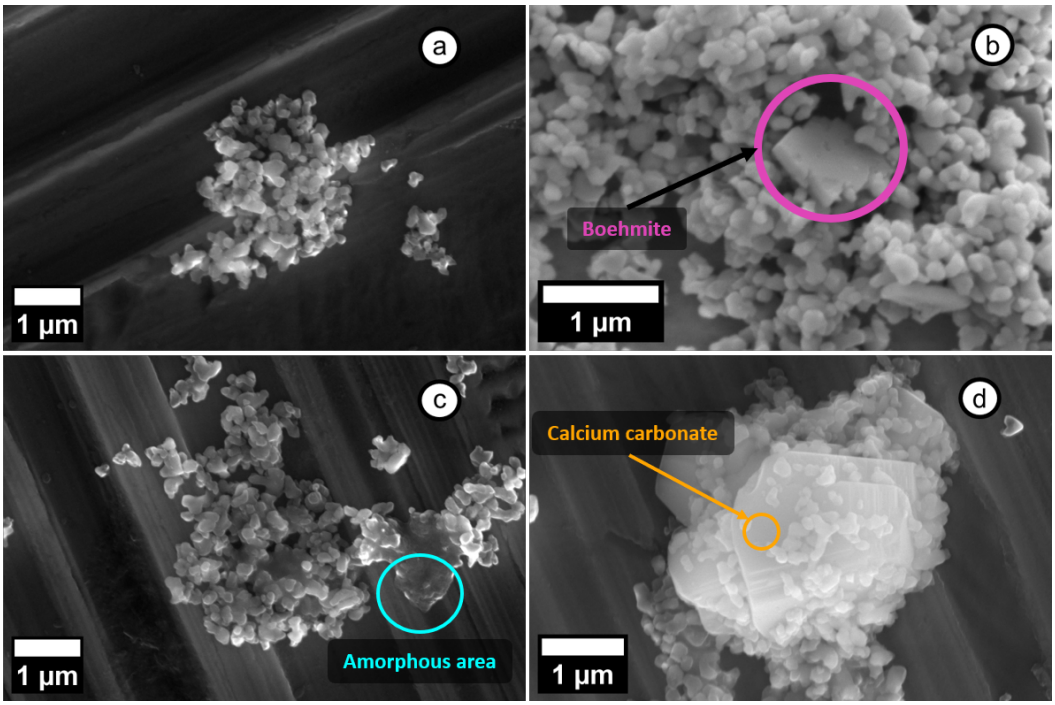


Figure 12. SEM-EDX images of solid phases. (**a**) Initial alumina powder (150 nm grains). (**b**) Alumina aged for 30 days at 150 °C (***P150***, stirred): boehmite grains (pellet-like morphology). (**c**) Alumina aged for 220 days at 70 °C (***P70***, static): amorphous hydrated phase (O:Al:C:S:K = 57:14:21:3:5). (**d**) Neoformed calcium carbonate precipitate from ***P70*** (Ca:C:O = 20:26:54).

The morphology, composition, and crystalline structure of alumina powder aged at 150 °C (***P150***, stirred, 30 days) were characterised by TEM, EDX mapping, and electron diffraction (Figure 13). TEM images reveal boehmite grains with a pellet-like morphology, 20 nm thick and 200–400 nm long (Figure 13a). The boehmite phase is confirmed by electron diffraction in the zone axis [1 −1 2] (Figure 13b). EDX mapping shows the spatial distribution of oxygen (Figure 13c), aluminium (Figure 13d), and silicon (Figure 13e), revealing a Si–rich surface layer on the boehmite grains with an Al/Si atomic ratio of 97.5/2.5.

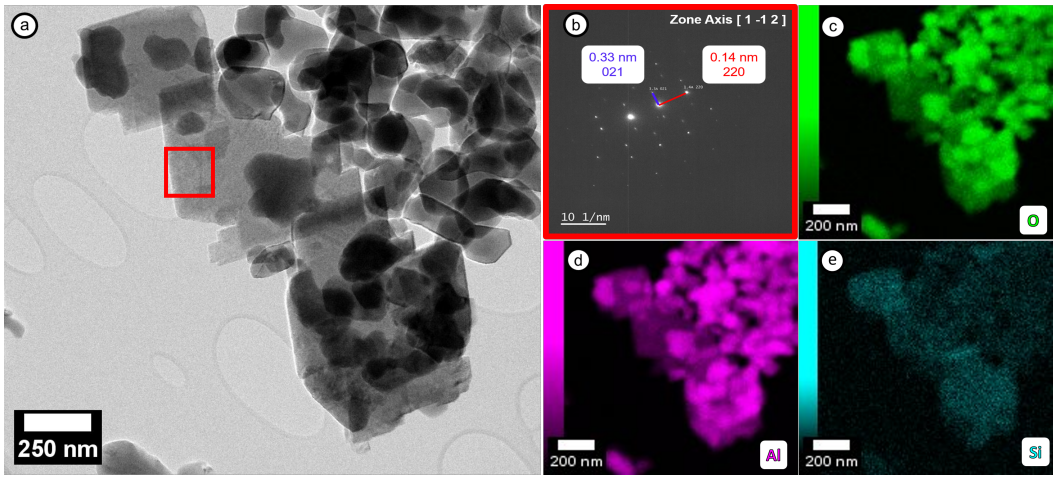


Figure 13. TEM, EDX mapping, and electron diffraction analysis of alumina powder aged at 150 °C (***P150***, stirred, 30 days). (**a**) TEM image: boehmite grains with pellet-like morphology (20 nm thick, 200–400 nm long; scale bar: 250 nm). (**b**) Electron diffraction pattern: boehmite phase confirmed in zone axis [1 −1 2]. (**c**) EDX mapping: oxygen (O) distribution. (**d**) EDX mapping: aluminium (Al) distribution. (**e**) EDX mapping: silicon (Si) distribution.

3.2.3. Initial and Aged Alumina Fibres

The concentrations of different species in the aqueous solution, determined by ICP (Figure 7), are affected differently by the presence of the alumina fibres in experiment ***F70***. The calcium, potassium, and sodium concentrations are equivalent to those in the initial aqueous solution. The silicon concentration is approximately 83% and decreases over time from 2.1 mmol·L^{-1} to 0.36 ± 0.02 mmol·L^{-1}. The rest is transferred to the solid phases. The aluminium concentration is 87% and decreases over time from 0.04 mmol·L^{-1} to 0.0042 ± 0.0002 mmol·L^{-1}.

Figure 8a indicates that the pH of the aqueous solution in contact with the alumina fibres follows the same initial trend as the solution alone during the first 3 days. Afterward, the pH decreases less rapidly and even appears to shift to a slower regime on the fourth day. At 220 days, the pH is 10.16, which is 0.7 pH units higher than that of the solution alone or in contact with the powder. However, as shown in Figure 8b, the thermodynamic pH for the fibres/aqueous solution system is predicted to be 5.28, which is far from the observed value.

Figure 14 shows SEM images of the initial and aged fibres. Initially, the fibre surface is smooth and exhibits no visible roughness (Figure 14a). In experiment ***F70*** (70 °C for 220 days), the surface begins to show slight roughness due to the presence of a thin layer on the fibres (Figure 14b). In experiment ***F150*** (150 °C for 30 days), the surface morphology is modified by a continuous coverage of particles observed along the entire fibre (Figure 14c). This reflects a gradual increase in surface roughness with ageing, increasing with higher temperatures.

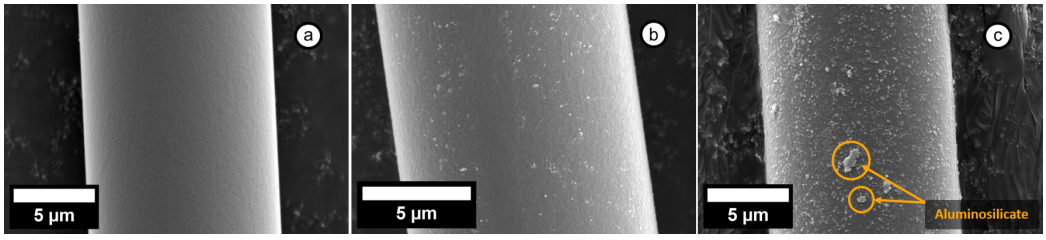


Figure 14. SEM images of alumina fibres. (**a**) Initial fibre (smooth surface). (**b**) ***F70*** (220 days, 70 °C, static): slight roughness. (**c**) ***F150*** (30 days, 150 °C, stirred): continuous particle coverage.

XPS analysis of the alumina fibres provides insights into the surface composition and its evolution upon ageing. The XPS spectrum at the surface of the initial fibres (Figure 15a) shows a characteristic Al 2p peak at 74 eV, along with O 2s electrons, while silicon is barely detectable due to its low initial content (0.3 $\%_m$). After ageing at 70 °C for 220 days in experiment ***F70***, the Si 2p peak (102–103 eV) becomes more intense than the Al 2p peak (Figure 15a), indicating the formation of a Si-rich surface layer. The energy of the Si 2p peak (102–103 eV) suggests that silicon atoms are not in a silica-like environment (typically 104–105 eV), but rather in an aluminosilicate phase. The presence of carbon and sodium after ageing is attributed to the deposition of secondary phases such as sodium sulfate and calcium carbonate.

Depth profiling by XPS (Figure 15b) reveals further details about the compositional changes. The oxygen content remains relatively constant with depth, whereas the aluminium concentration increases progressively with sputtering time. For the aged fibres, the aluminium signal reaches a value close to that of the initial fibres only after 600 s of sputtering, indicating the presence of a homogeneous Si–rich sublayer at the surface. The silicon content reaches up to 28% at the surface and decreases steadily with depth but does not fall to zero even after extended sputtering. This residual signal is attributed to the fibrous and woven nature of the sample, where the analysis volume may still include contributions from overlapping or surface-exposed fibres.

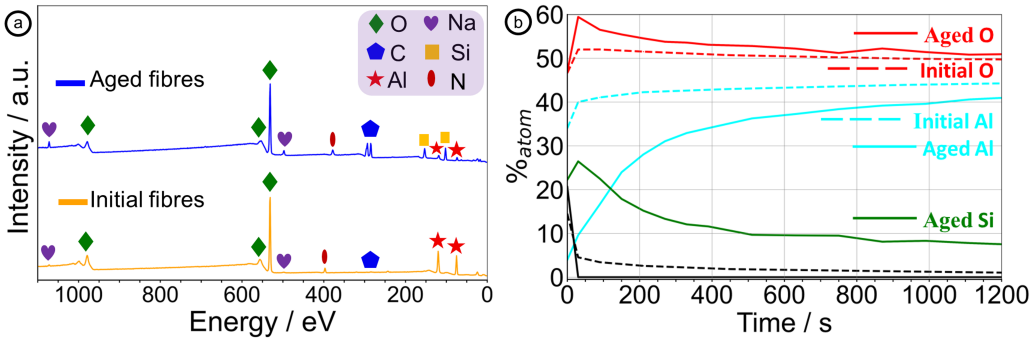


Figure 15. XPS analysis of alumina fibres. (**a**) XPS spectra at the surface: initial fibres (orange) show *Al* 2p (74 eV) and *O* 2s peaks, while aged fibres (***F70***, blue) exhibit a *Si* 2p peak (102–103 eV), indicating a *Si*-rich surface layer. (**b**) Depth profiling: atomic % vs. sputtering time for initial fibres (dashed lines) and aged fibres (***F70***, solid lines). The *Si* content reaches 28% at the surface and decreases with depth, while *Al* increases progressively.

Figure 16 shows the TEM images of the alumina fibres before and after ageing. Initially, the fibre is composed of alumina grains, with an average diameter of 70 nm, and nanoporosities (Figure 16a). The alumina fibres aged for 220 days and 30 days at 70 °C and 150 °C in experiments ***F70*** and ***F150*** exhibit a crystallised core with grain diameters of about 70 nm, as in the initial fibre. Nanoporosities are still present. There is a nanolayer of about 20 nm that is formed at the surface. This layer is present over the entire surface of the fibre and is homogeneous.

Figure 17 shows the EDX analysis of the fibres aged at 70 °C and 150 °C in experiments ***F70*** and ***F150***. The layer formed on the aged fibres contains both silicon and aluminium, confirming the formation of an aluminosilicate layer, as also observed by XPS (Figure 15).

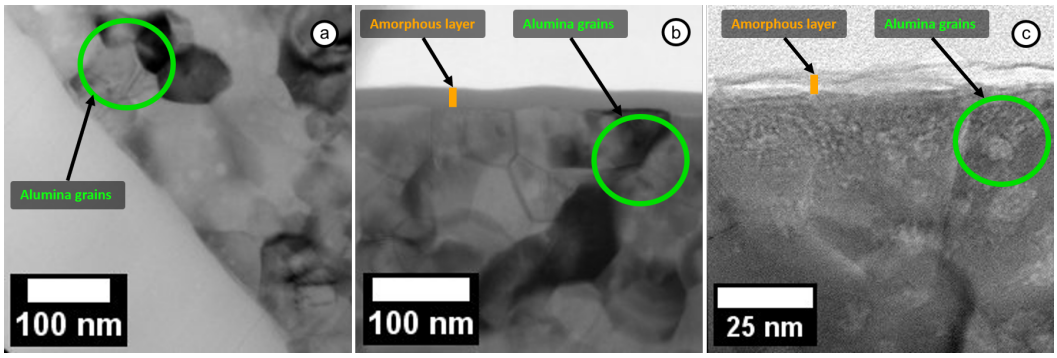


Figure 16. TEM images of alumina fibres. (**a**) Initial fibre (70 nm grains, nanoporosity). (**b**) ***F70*** (220 days, 70 °C, static): 20 nm homogeneous surface layer. (**c**) ***F150*** (30 days, 150 °C, stirred): same layer observed.

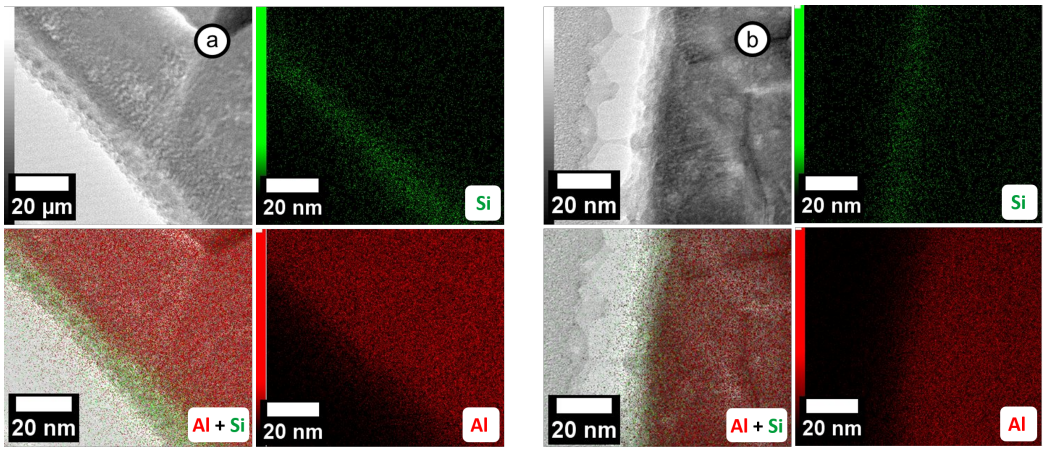


Figure 17. EDX analysis of alumina fibres. (**a**) ***F70*** (220 days, 70 °C, static): Si–Al-rich surface layer. (**b**) ***F150*** (30 days, 150 °C, stirred): same layer composition.

4. Discussion

The combination of thermodynamic calculations and experimental characterisations allows key differences to be identified under hydrothermal alkaline conditions in the behaviour of alumina with respect to its morphology, i.e., powder or fibres, and depending on the ageing conditions (T, t, stirring). The analysed systems do not reach complete thermodynamic equilibrium but evolve towards para-equilibrium states, where reaction kinetics and interfacial interactions control the evolution pathways.

For aqueous ageing without the addition of solids, thermodynamic calculations predict the precipitation of sodium sulfate (Na_2SO_4), gypsum ($CaSO_4{\cdot}2H_2O$), and calcium silicate (Ca_2SiO_4) (Figure 1), which is close to the experimental observations. First, the ICP data show an almost complete precipitation of calcium into carbonate (Figures 7a and 10a). Second, sodium and potassium remain mainly in solution, although precipitation of a mixed alkali sulfate ($KNaSO_4$) is confirmed by XRD (Figure 10a). Third, the aluminium concentration in the leaching solution increases by about 80% over time, indicating the dissolution of the aluminosilicate phase identified by TEM coupled with an EDX probe (Figure 9). Thermodynamically, the aluminium present in the solution should precipitate as diaspore (α–AlOOH) in a stable system or as boehmite (β–AlOOH) in a metastable system at low temperatures and then as calcium aluminosilicate ($Ca_2Al_2SiO_7$) at higher temperatures. This shows that the regime established for aluminium is one of dissolution rather than hydration or reprecipitation.

With regard to the ageing of alumina powder, a clear contrast appears between the conditions at 70 °C (***P70***) and those at 150 °C (***P150***). At 70 °C, the experimental

aluminium concentration is 2.8 times higher than that of the initial solution, confirming the partial dissolution of the alumina powder. However, no hydrated alumina phase is detected, such as diaspore or boehmite. This observation is consistent with results available in the literature, particularly those of Chen et al., who emphasised that agitation of the system is a determining factor in the transformation of alumina into a hydrated phase, regardless of pH [14]. Thermodynamic calculations indicate that boehmite or diaspore should precipitate depending on the stability of the system (Figure 2), with a limited effect on the rest of the composition of the system, but the absence of such phases in the experiments suggests that the system remains in a kinetically controlled regime. Under static conditions, a stagnant diffusion layer forms in the area of the alumina grains. This zone is subjected to a local accumulation of dissolution products, such as $Al(OH)_4^-$ aluminate species and hydroxide (OH^-) reactants. This high local saturation and relatively low temperature affect the kinetics of alumina transformation, limiting both the initial dissolution of alumina and the secondary precipitation into hydrated phases. This phenomenon can be explained by Le Chatelier's principle: the chemical system tends to oppose the applied disturbance (accumulation of dissolved products) by shifting the equilibrium direction, i.e., by slowing down or even blocking the dissolution and hydration of alumina. In the absence of mechanical convection, the dissolved species are not renewed around the particles, which freezes this state of local imbalance. In addition, the precipitated particles can cover the surface of the alumina powder, also limiting exchange phenomena. These simultaneous effects severely limit the transformation mechanisms of alumina, which remain dominated by the simple accumulation of external precipitates from the leaching medium, such as carbonates or sulfates, as observed in XRD and SEM imaging (Figures 10a and 12). A rough estimate of the kinetics of dissolution of alumina was made based on the total aluminium measured in solution at 70 °C. The dissolution rate is approximated as 2.95×10^{-3} mg·m^{-2}·day^{-1}, indicating a slow alteration of alumina under these conditions.

At 150 °C under agitated conditions (***P150***), the alumina powder undergoes a clear transformation to boehmite, identified by XRD (Figure 10b) and TEM (Figure 13a), and confirmed by electron diffraction (Figure 13b). EDX mapping reveals a Si-rich surface layer on the boehmite grains (Al/Si = 97.5/2.5; Figure 13d,e). The growth of boehmite over time, monitored by Rietveld refinement of XRD patterns (Figure 11), suggests a dissolution-hydration mechanism favoured by the continuous renewal of species at the interface. Thermodynamic calculations confirm that boehmite is a metastable phase, while diaspore is the most stable (lowest Gibbs free energy at a given temperature). Although chemically identical, these two polymorphs differ in structure: diaspore has a dense three-dimensional stack of octahedra, whereas boehmite is organised in sheets linked by hydrogen bonds [39,40]. This structure makes boehmite less dense and more reactive, making it a metastable phase. The formation of boehmite instead of diaspore is attributed to kinetic control. The small difference in Gibbs free energy between the two polymorphs (going from ΔG = 640 J·mol^{-1} at 70 °C to ΔG = 556 J·mol^{-1} at 150 °C), combined with high temperature and dynamic mixing, favours the formation of the less stable but more easily accessible phase.

For fibres at 70 °C (***F70***), ICP measurements show a significant decrease in silicon and aluminium concentrations in the solution, with more than 80% of the silicon of the aqueous solution transferring into the solid phase. Thermodynamic calculations predict a final silicon concentration of 4 mmol·L^{-1} at 70 °C in the system with $x_{Al_2O_3} + x_{SiO_2} = 0.05$, but experimentally, only 0.357 mmol·L^{-1} remains in solution. This significant discrepancy confirms that silicon is precipitated in aluminosilicate phases. XPS and TEM-EDX analyses (Figures 15 and 17) show the formation of a homogeneous surface layer (20 nm) enriched

in aluminium and silicon. The fibres thus act as a preferential substrate for the nucleation of aluminosilicates. The silicon content of the fibres contributes to this precipitation process. At 150 °C (***F150***), the same layer of aluminosilicates is observed, suggesting a precipitation mechanism independent of temperature. Thermodynamic calculations at $x_{Al_2O_3} + x_{SiO_2} = 0.05$ indicate stable precipitation of muscovite and kaolinite at low temperatures and carnegieite and C4AsH12 ($CaO{\cdot}Al_2O_2{\cdot}CaSO_4{\cdot}12H_2O$) at higher temperatures (Figure 3), all of which are solids containing silicon and aluminium. This confirms a strong interaction between the solid surface and soluble silicon species, leading to the gradual formation of a silicate layer on the surface.

Changes in the pH of the systems provide further insight into the reaction mechanisms. As shown in Figure 8, the pH of the aqueous solution alone decreases from 10.88 to 9.87 over 220 days, indicating that the solution-only system has not reached equilibrium and continues to evolve. The presence of alumina powder initially accelerates this pH decrease, probably due to the dissolution of species on the surface of the alumina. However, the pH stabilises at around 9.89, a value almost equal to that of the solution alone, suggesting that the dissolution of the alumina is limited by the formation of a stagnant diffusion layer, as mentioned previously. In contrast, the pH of the solution in contact with the alumina fibres decreases more slowly, reaching only 10.16 after 220 days. This behaviour can be explained by the formation of a protective aluminosilicate layer on the fibre surface, which reduces the direct interaction between the fibre surface (alumina and silica) and the solution, thereby slowing down both the dissolution and the decrease in pH. The discrepancy between the experimental pH (10.16) and the thermodynamic prediction (5.28) for the fibre-based system confirms that the system is far from equilibrium, likely due to the kinetic barriers imposed by the surface layer and the absence of agitation.

Comparison of the behaviour of the powder and fibres reveals significant differences. While alumina powder mainly dissolves in the leaching solution at 70 °C and precipitates as boehmite at 150 °C under kinetically favourable conditions, the fibres favour the formation of aluminosilicate layers, regardless of temperature. This can be explained by differences in surface chemistry, morphology, or the presence of initial silicate in the fibres. The thermodynamic calculations assume infinite reaction time and ideal mixing conditions, which explains the deviations from the experimental results for the aqueous solution, powder/solution, and fibre/solution systems. Overall, the discrepancies between the thermodynamic predictions and experimental observations reveal the strong influence of kinetic constraints (slow and complex evolution involving multiple transitional stages), interface-specific reactions, and material-dependent behaviour. While thermodynamic calculations identify the possible final states, the actual evolution of the system remains determined by transport, nucleation, and surface affinity effects. Experiments thus capture intermediate stages of para-equilibrium, where metastable phases such as boehmite and amorphous aluminosilicates dominate the systems.

5. Conclusions

This work examined the physico-chemical stability over time at 70 °C and 150 °C, with and without stirring, of different forms of alumina (powder and fibres) in a complex aqueous alkaline solution, using a combination of experimental analytical characterisation methods (ICP, XRD, SEM, XPS, TEM-EDX) and thermodynamic calculations. The results show that the initial solution evolves over time through the precipitation of different solid phases, such as sodium and potassium sulfates, calcium carbonate, and aluminosilicates, some of which are amorphous or metastable. Alumina powder interacts with the aqueous medium, leading to the formation of boehmite phases, whereas thermodynamic calculations predict the formation of diaspore. This discrepancy illustrates the importance of

kinetic and structural effects in the formation of secondary phases. The analyses also revealed differences in the behaviour of silicon as a function of alumina morphology, with precipitation being more notable in the case of fibres, suggesting specific interactions at the solid–liquid interface. In addition, the precipitated phases (sulfates, carbonates, aluminosilicates) indicate a continuous evolution of the system towards equilibrium, but without reaching it completely, even after several months. All these observations highlight the complexity of the system and the interactions between the components of the CMC in hyperalkaline environments. Additionally, data on pH changes reveal that chemical interactions within these systems are influenced by both the morphology of the alumina and the formation of secondary phases. The slower decrease in pH in the presence of fibres compared to powder suggests that the formation of a protective aluminosilicate layer mitigates dissolution, thereby preserving the structural integrity of the fibres. This behaviour indicates that alumina fibre-based CMCs could offer good long-term resistance under storage conditions. However, further studies are needed to confirm whether this protective layer persists over extended time scales and to assess its influence on the mechanical behaviour of the fibres. Nevertheless, the minor changes observed suggest that alumina powder and fibres are suitable candidates for waste storage. The next step will be to conduct ageing tests on the composite under these conditions to determine whether the material retains its mechanical properties.

Author Contributions: Conceptualization, J.R., E.P., F.R., A.D. and X.B.; methodology, G.G., E.P., F.R. and J.R.; formal analysis, G.G. and J.R.; validation, E.P., F.R., A.D., X.B. and J.R.; investigation, G.G. and J.R.; writing—original draft preparation, G.G.; writing—review and editing, G.G. and J.R.; supervision, E.P., F.R. and J.R. All authors have read and agreed to the published version of the manuscript.

Funding: This research received no external funding.

Data Availability Statement: The data presented in this study are available on request from the corresponding author.

Acknowledgments: This work is the result of collaboration between the Thermostructural Composites Laboratory (LCTS), IRT Saint Exupéry, and the French National Radioactive Waste Management Agency (Andra). This research was supported by the French National Research Agency (ANR).

Conflicts of Interest: The authors declare no conflicts of interest.

References

1. McCartin, T.; Tadesse, R.; Li, J.; Umeki, H.; Bilbao y Leon, S.; Palos, G. *Management and Disposal of High-Level Radioactive Waste: Global Progress and Solutions*; Organisation for Economic Co-Operation and Development: Paris, France, 2020.
2. Andra. Submission Application Authorization Create Cigéo. 2023. Available online: https://international.andra.fr/submission-application-authorization-create-cigeo (accessed on 5 November 2024).
3. Crusset, D.; Deydier, V.; Necib, S.; Gras, J.-M.; Combrade, P.; Féron, D.; Burger, E. Corrosion of Carbon Steel Components in the French High-Level Waste Programme: Evolution of Disposal Concept and Selection of Materials. *Corros. Eng. Sci. Technol.* **2017**, *52*, 17–24. [CrossRef]
4. Bumbieler, F.; Plúa, C.; Tourchi, S.; Vu, M.-N.; Vaunat, J.; Gens, A. Feasibility of Constructing a Full-Scale Radioactive High-Level Waste Disposal Cell and Characterization of Its Thermo-Hydro-Mechanical Behavior. *Int. J. Rock Mech. Min. Sci.* **2021**, *137*, 104555. [CrossRef]
5. Camus, G.; Lorrette, C.; Pailler, R.; Rebillat, F.; Reignier, B.; Teyssandier, F. *Matériaux Composites à Matrice Céramique et à Renfort par Fibres Longues*; Editions TI: Paris, France, 2016.
6. Debelle, A.; Besnard, C.; Miot, S.; Perret, E.; Couillaud, S.; Ganster, P.; Rossignol, F.; German, G.; Reine, B.; Pasteau, A.; et al. Ceramics as Alternative Solutions for the Geological Disposal of High-Level Radioactive Waste: Andra's R&D Program. *Int. J. Appl. Ceram. Technol.* **2025**, *22*, e15022. [CrossRef]
7. Perret, E.; Miot, S.; Box, M.; D'Elia, R. 111. Patent FR3115533A1, 24 November 2023. [CrossRef]

8. Pignatelli, I.; Bourdelle, F.; Bartier, D.; Mosser-Ruck, R.; Truche, L.; Mugnaioli, E.; Michau, N. Iron–Clay Interactions: Detailed Study of the Mineralogical Transformation of Claystone with Emphasis on the Formation of Iron-Rich T–O Phyllosilicates in a Step-by-Step Cooling Experiment from 90 °C to 40 °C. *Chem. Geol.* **2014**, *387*, 1–11. [CrossRef]
9. Suchanek, W.L. Hydrothermal Synthesis of Alpha Alumina (α-Al_2O_3) Powders: Study of the Processing Variables and Growth Mechanisms. *J. Am. Ceram. Soc.* **2010**, *93*, 399–412. [CrossRef]
10. Serena, S.; Raso, M.A.; Rodriguez, M.A.; Caballero, A.; Leo, T. J. Thermodynamic Evaluation of the Al_2O_3–H_2O Binary System at Pressures up to 30 MPa. *Ceram. Int.* **2009**, *35*, 3081–3090. [CrossRef]
11. Al'Myasheva, O.V.; Korytkova, E.N.; Maslov, A.V.; Gusarov, V.V. Preparation of Nanocrystalline Alumina under Hydrothermal Conditions. *Inorg. Mater.* **2005**, *41*, 460–467. [CrossRef]
12. Laubengayer, A.W.; Weisz, R.S. A Hydrothermal Study of Equilibria in the System Alumina—Water. *J. Am. Chem. Soc.* **1943**, *65*, 247–250. [CrossRef]
13. Ervine, G., Jr.; Osborn, E.F. The System Al_2O_3–H_2O. *J. Geol.* **1951**, *59*, 381–394. [CrossRef] [PubMed]
14. Chen, Y.; Hyldtoft, J.; Jacobsen, C.J.H.; Nielsen, O.F. NIR FT Raman Spectroscopic Studies of η-Al_2O_3 and Mo/η-Al_2O_3 Catalysts. *Spectrochim. Acta Part A* **1995**, *51*, 2161–2169. [CrossRef]
15. Carrier, X.; Marceau, E.; Lambert, J.-F.; Che, M. Transformations of γ-Alumina in Aqueous Suspensions: Alumina Chemical Weathering Studied as a Function of pH. *J. Colloid Interface Sci.* **2007**, *308*, 429–437. [CrossRef] [PubMed]
16. Roelofs, F.; Vogelsberger, W. Dissolution Kinetics of Nanodispersed γ-Alumina in Aqueous Solution at Different pH: Unusual Kinetic Size Effect and Formation of a New Phase. *J. Colloid Interface Sci.* **2006**, *303*, 450–459. [CrossRef] [PubMed]
17. Bureau de Recherches Géologiques et Minières (BRGM). *Projet SYNTHÈSES EAUX: Protocoles de Synthèse de Fluides Représentatifs de Différentes Configurations de L'alvéole HA*; BRGM/RP-66357-FR; BRGM: Orléans, France, 2017.
18. Andersson, J.-O.; Helander, T.; Höglund, L.; Shi, P.; Sundman, B. Thermo-Calc & DICTRA, Computational Tools for Materials Science. *Calphad* **2002**, *26*, 273–312. [CrossRef]
19. Lukas, H.; Fries, S.G.; Sundman, B. *Computational Thermodynamics: The Calphad Method*; Cambridge University Press: Cambridge, UK, 2007.
20. Thermo-Calc Software. GCE2 Mineral Database. 2024. Available online: https://thermocalc.com/products/databases/minerals/ (accessed on 5 November 2024).
21. Thermo-Calc Software. TCAQ3 Aqueous Solutions Databases. 2024. Available online: https://thermocalc.com/products/databases/aqueous-solutions/ (accessed on 5 November 2024).
22. Thermo-Calc Software. TCOX13 Metal Slag and Oxides Database. 2024. Available online: https://thermocalc.com/products/databases/metal-oxide-solutions/ (accessed on 5 November 2024).
23. Kim, D.-G.; Konar, B.; Jung, I.-H. Thermodynamic Optimization of the K_2O-Al_2O_3-SiO_2 System. *Ceram. Int.* **2018**, *44*, 16712–16724. [CrossRef]
24. Lothenbach, B.; Pelletier-Chaignat, L.; Winnefeld, F. Stability in the System CaO–Al_2O_3–H_2O. *Cem. Concr. Res.* **2012**, *42*, 1621–1634. [CrossRef]
25. Utlak, S.A.; Besmann, T.M. Thermodynamic Assessment of the Na_2O-Al_2O_3-SiO_2-B_2O_3 Pseudo-Binary and -Ternary Systems. *J. Chem. Thermodyn.* **2019**, *130*, 251–268. [CrossRef]
26. Hallstedl, B. Assessment of the CaO-Al_2O_3 System. *J. Am. Ceram. Soc.* **1990**, *73*, 15–23. [CrossRef]
27. Gottschalk, M. Internally Consistent Thermodynamic Data for Rock-Forming Minerals in the System SiO_2-TiO_2-Al_2O_3-CaO-MgO-FeO-K_2O-Na_2O-H_2O-CO_2. *Eur. J. Mineral.* **1997**, *9*, 175–223.
28. Yaokawa, J.; Oikawa, K.; Anzai, K. Thermodynamic Assessment of the KCl–K_2CO_3–NaCl–Na_2CO_3 System. *Calphad* **2007**, *31*, 155–163. [CrossRef]
29. Lothenbach, B.; Matschei, T.; Möschner, G.; Glasser, F.P. Thermodynamic Modelling of the Effect of Temperature on the Hydration and Porosity of Portland Cement. *Cem. Concr. Res.* **2008**, *38*, 1–18. [CrossRef]
30. Holland, T.J.B.; Powell, R. An Improved and Extended Internally Consistent Thermodynamic Dataset for Phases of Petrological Interest, Involving a New Equation of State for Solids. *J. Metamorph. Geol.* **2011**, *29*, 333–383. [CrossRef]
31. Matsuo, K. Thermodynamic Modelling of the CaO-SiO_2-H_2O Cementitious System & the Production of Waste-Derived Cement. Master's Thesis, McGill University, Montréal, QC, Canada, 2017.
32. Kim, D. Coupled Experimental Study and Thermodynamic Optimization of the K_2O-Na_2O-CaO-MgO-Al_2O_3-SiO_2 System. Ph.D. Thesis, McGill University, Montréal, QC, Canada, 2017.
33. Nekhoroshev, E. Thermodynamic Optimization of the Na_2O-K_2O-Al_2O_3-CaO-MgO-B_2O_3-SiO_2 System. Ph.D. Thesis, École Polytechnique de Montréal, Montréal, QC, Canada, 2019.
34. Yazhenskikh, E.; Jantzen, T.; Kobertz, D.; Hack, K.; Mueller, M. Critical Thermodynamic Evaluation of the Binary Sub-Systems of the Core Sulphate System Na_2SO_4–K_2SO_4–$MgSO_4$–$CaSO_4$. *Calphad* **2021**, *72*, 102234. [CrossRef]
35. Linstrom, P.J.; Mallard, W.G. *NIST Chemistry WebBook, NIST Standard Reference Database Number 69*; National Institute of Standards and Technology: Gaithersburg, MD, USA, 2011.

36. Thermo-Calc Software. The TC-Python API Programmer Guide 2024b. 2024. Available online: https://thermocalc.com/support/documentation/ (accessed on 5 November 2024).
37. Ramaswamy, R.; Yliniemi, J.; Illikainen, M. Dissolution-Precipitation Reactions of Silicate Mineral Fibers at Alkaline pH. *Cem. Concr. Res.* **2022**, *160*, 106922. [CrossRef]
38. Brady, P.V.; Walther, J.V. Controls on Silicate Dissolution Rates in Neutral and Basic pH Solutions at 25 °C. *Geochim. Cosmochim. Acta* **1989**, *53*, 2823–2830. [CrossRef]
39. Ervine, F.J. The Crystal Structure of Diaspore. *J. Chem. Phys.* **1935**, *3*, 203–207. [CrossRef]
40. Ervine, F.J. The Crystal Structure of Lepidocrocite. *J. Chem. Phys.* **1935**, *3*, 420–424. [CrossRef]

Disclaimer/Publisher's Note: The statements, opinions and data contained in all publications are solely those of the individual author(s) and contributor(s) and not of MDPI and/or the editor(s). MDPI and/or the editor(s) disclaim responsibility for any injury to people or property resulting from any ideas, methods, instructions or products referred to in the content.